

奈米碳管與氧化鈦奈米點之陽極氧化鋁模板輔助成長 與電子場效發射

研究生：陳柏林

指導教授：郭正次 教授

潘扶民 教授

國立交通大學

材料科學與工程學系博士班

摘要

本研究利用奈米多孔性的陽極氧化鋁薄膜作為模板輔助成長奈米碳管與氧化鈦奈米點之規則陣列並探討其電子場效發射性質。具有規則排列奈米孔洞的陽極氧化鋁乃由熱蒸鍍鋁膜之兩階段陽極氧化處理所得，而奈米碳管乃以微波電漿電子迴旋共振化學氣相沈積法成長於陽極氧化鋁薄膜的奈米孔洞內。奈米碳管的成長受到奈米孔洞的限制與外加偏壓或電漿自我偏壓的影響，因而具有極佳的垂直準直性。電子場效發射量測顯示陽極氧化鋁輔助成長的奈米碳管陣列具有優異的場發射性質，歸因於其均勻的尺寸分佈、極佳的準直性與高度的石墨化等特性。由於奈米碳管之管束密度對其電子場效發射具有關鍵性的影響，因此，本研究提出一簡單且可靠的方法進行控制奈米碳管之管束密度。藉由調整甲烷與氫氣之反應氣體比例即可有效地控制奈米碳管成長出奈米孔洞外之管束密度。此方法乃利用奈米碳管成長與非晶質碳覆蓋奈米孔洞此二反應之間的動態競爭。隨著增加反應氣氛之甲烷濃度，非晶質碳附產物之沈積速率增加，因而有效減少能即時成長出孔洞外之奈米碳管的數量。當甲烷濃度由 9% 增加至 91%，奈米碳管之管束密度降低達 4.5 倍。因為緩和了場遮蔽效應，奈米碳管之場效發射性質因降低管束密度而大幅提昇，然而，在高甲烷濃度的成長條件下，非晶質碳附產物亦會沈積於奈米碳管表面引起額外的能障與電壓降，造成電子場效發射性質顯著的退化。

高度規則排列的氧化鈦奈米點陣列可直接由鋁與氮化鈦雙層薄膜之陽極氧化處理獲得。氮化鈦薄膜之陽極氧化被侷限於首先形成之陽極氧化鋁奈米孔洞內，

因而得到奈米尺度的島狀氧化鈦陣列。奈米點之排列與形狀能如實的複製陽極氧化鋁模板之奈米孔洞，且奈米點之尺寸可藉由調整陽極處理之參數準確的控制。若採用磊晶的鋁與氮化鈦雙層薄膜將可更進一步改善奈米點的尺寸均勻度與表面平整度。此新穎的技術極具潛力可應用於製作各種氧化物半導體奈米點的規則陣列。此外，研究結果顯示氧化鈦奈米點之相變化行為與一般氧化鈦薄膜或粉末大異其趣。經過高溫退火後，奈米點為銳鈦礦介穩相與金紅石穩定相的多晶所組成。由於高溫結晶化的過程被限制於孤立的奈米島狀結構內，氧化鈦之晶粒成長與相變化受到阻礙，導致銳鈦礦介穩相在高溫下仍能穩定存在於氧化鈦奈米點內。本研究亦利用奈米點作為電子發射源製作場效發射三極體元件。此場效發射三極體擁有 45 伏特之低閘極啟始電壓，且在 120 伏特的閘極電壓下，場效發射電流密度高達 25 毫安培/平方公分。此奈米點之電子發射源具有低製程溫度與極佳的均勻性等優點，將可滿足大面積場效發射顯示器之製程需求。



Anodic aluminum oxide template assisted growth and electron field emission of carbon nanotubes and titanium oxide nanodots

Student: Po-Lin Chen

Advisors: Prof. Cheng-Tzu Kuo
Prof. Fu-Ming Pan

Department of Materials Science and Engineering
National Chiao Tung University

Abstract

Ordered arrays of carbon nanotubes (CNTs) and titanium oxide (TiO_2) nanodots have been successfully prepared by using the nanoporous anodic aluminum oxide (AAO) films as templates. Nanoporous AAO templates with hexagonal pore arrangement were prepared by the two-step anodization of aluminum films. Highly aligned CNTs were grown in vertical channels of the AAO template by microwave plasma electron cyclotron resonance chemical vapor deposition (ECR-CVD). The segments of CNTs stretching out of the AAO nanopores still maintain relatively good alignment, and have a very slow growth rate, which allows us to obtain reproducible tube length by tuning the growth time. Field emission measurements of the CNTs showed good electron emission properties, attributed to their uniformity in size, good alignment, and good graphitization properties. We have also demonstrated that the tube number density of aligned CNTs grown over the AAO template can be directly controlled by adjusting the $\text{CH}_4:\text{H}_2$ feed ratio during the CNT growth. We ascribe the variation of the tube density as a function of the $\text{CH}_4:\text{H}_2$ feed ratio to the kinetic competition between outgrowth of CNTs from the AAO pore bottom and deposition of the amorphous carbon overlayer on the AAO template. A pore-filling ratio of 18 to 82% for the nanotubes overgrown out of nanopores on the AAO template can be easily achieved by adjusting the $\text{CH}_4:\text{H}_2$ feed ratio. Enhanced field emission properties of CNTs were obtained by lowering the tube density on AAO. However, at a high CH_4 concentration, amorphous carbon byproduct deposit on the CNT surface can degrade the field emission property due to a high energy barrier and significant potential drop at the emission site.

Highly ordered nanodot arrays of TiO₂ were prepared from Al/TiN films on the silicon substrate by electrochemical anodization of a TiN layer using a nanoporous AAO film as the template. The arrangement and shape of the nanodots are in accordance with the nanopores of the AAO template. The size of the nanodots can be varied over a wide range (ten to several hundred nanometers) because the diameter of the AAO nanopores is dependent upon anodization parameters. The size uniformity and surface smoothness of the TiO₂ nanodots can be further improved by anodization of an epitaxial Al/TiN film stack on a sapphire substrate. The phase development of the isolated TiO₂ nanodots is very much different from TiO₂ thin films and powders. After high temperature annealing, the nanodots are polycrystalline and consist of a mixed phase of anatase and rutile instead of single rutile phase. We conclude that TiO₂ nanodots with a single phase of anatase can be realized as long as the size of the nanodots is smaller than the critical nuclei size for rutile formation. Using this novel approach, it is expected that nanodot arrays of various oxide semiconductors can be achieved. Furthermore, a field emission triode device using the self-organized nanodot arrays as electron emission source was proposed and fabricated. The field emission triodes with nanodot emitters exhibited a low gate turn-on voltage of 45 V and high emission current density of 25 mA/cm² at 120 V. The desirable electric properties and easily controllable fabrication process of the nanodot triodes show potential for application in field emission displays (FEDs) and vacuum microelectronics.

Acknowledgements

首先，筆者由衷地感謝指導教授郭正次教授與潘扶民教授四年來辛勤的指導與教誨，並且在待人處世方面給予莫大的啟發，使我畢生受益匪淺，謹此致以最誠摯的謝意。感謝清大材料系陳力俊教授、交大材料系陳家富教授、中央機械系林景崎教授、中興材料系薛富盛教授、成大化工系洪昭南教授與成大機械系李驊登教授等考試委員的蒞臨指導。筆者亦由衷地感謝蔡增光博士，因為您的寶貴意見，使得本論文能順利完成。此外，筆者要特別感謝北科大陳志恆教授，有您的啟蒙與鼓勵，我才得以攻讀博士學位。

感謝兆勳學長與威翔學長對本論文提供寶貴的建議。感謝峻愷，有你的協助，研究才能順利完成。謝謝瓊姿、穩駿、恩宗、智明、國仁、滷蛋與穎超等人在實驗上的協助與贊助。感謝李姐、俊翰、得山、祈廷、國銘、奕同、怡芬、貞君、必愷、祐君、伊茹、玉容、文綬學長、伯遠、安亞、榮倫、煌凱、崇獻與蔡豪等實驗室的伙伴們，謝謝你們在生活上的協助與鼓勵。感謝淑芸與系辦小姐們在行政上的協助。同時要感謝國科會提供研究經費、國家奈米元件實驗室提供研究設備與中華映管公司提供獎助學金。另外要感謝大學路的土地公，謝謝您的保佑。

最後，僅將本論文獻給我摯愛的老婆與家人，感謝你們的支持與鼓勵，使我順利得到博士學位。

Contents

Abstract (in Chinese).....	I
Abstract (in English).....	III
Acknowledgements.....	V
Contents.....	VI
List of symbols.....	VIII
Table Caption.....	X
Figure Caption.....	XI
Chapter 1 Introduction.....	1
1.1 Introduction to nanomaterials.....	1
1.2 Motivation.....	2
Chapter 2 Literature Review.....	6
2.1 Theoretical modeling of porous AAO formation.....	6
2.2 Synthesis methods of CNTs.....	9
2.3 Growth mechanisms for catalyst assisted CNTs.....	12
2.4 Nanofabrications of well aligned CNT arrays.....	15
2.5 Nanofabrication technologies of nanodot arrays.....	19
2.6 Basic field emission theory.....	24
2.7 Overview of cold cathode materials.....	26
2.8 Potential applications of field emission.....	28
Chapter 3 Experimental Methods.....	32
3.1 Experimental flowchart.....	32
3.2 Depositions of Al and TiN films.....	33
3.3 Electrochemical processes.....	34
3.4 Microwave plasma ECR-CVD system.....	35
3.5 Material analysis methods.....	36
3.6 Field emission measurement.....	38
Chapter 4 Self-Organized Nanopore Arrays of AAO Films.....	40
4.1 Introduction.....	40
4.2 Al film electropolishing.....	41
4.3 Two-step anodization.....	43

4.4 Summary.....	50
Chapter 5 Growth of AAO Assisted CNT Arrays.....	51
5.1 Introduction.....	51
5.2 Integration of AAO and CNTs.....	52
5.3 Field emission properties.....	57
5.4 Summary.....	59
Chapter 6 Tube Number Density Control of AAO Assisted CNT Arrays.....	60
6.1 Introduction.....	60
6.2 Mechanisms for tube density control.....	61
6.3 Field emission of tube density controlled CNTs.....	68
6.4 Summary.....	73
Chapter 7 Growth of Self-Organized TiO ₂ Nanodot Arrays.....	74
7.1 Introduction.....	74
7.2 Preparation and microstructure of TiO ₂ nanodots.....	75
7.3 Shape improvement of TiO ₂ nanodots.....	83
7.4 Phase stability of TiO ₂ nanocrystals.....	87
7.5 Phase development of TiO ₂ nanodots.....	89
7.6 Summary.....	92
Chapter 8 Applications of Nanodot Arrays in Field Emission Triodes.....	94
8.1 Introduction.....	94
8.2 Field emission from nanodot arrays.....	95
8.3 Fabrication and characterization of field emission triodes.....	99
8.4 Summary.....	102
Chapter 9 Conclusions.....	104
Chapter 10 Future Prospects.....	106
References.....	107
Vita.....	125

List of Symbols

- U_e : oxide/electrolyte interfacial speed
 U_m : metal/oxide interfacial speed
 α_1 : faradaic coefficient
 β_1 : faradaic coefficient
 γ_1 : faradaic coefficient
 A_1 : kinetic constant
 B_1 : kinetic constant
 k_d : kinetic constant
 k_0 : kinetic constant
 E_e : electric field strength at the oxide/electrolyte interface
 E_m : electric field strength at the metal/oxide interface
 E_b : base state electric field
 V_0 : applied voltage for aluminum anodization
 D_a : aluminum oxide thickness
 R : AAO pore radius
 R_0 : AAO pore radius extrapolated to $pH = 0$
 k : a function of k_0 , k_d , α_1 , β_1 , and γ_1
 $\Delta\phi$: decrease in barrier height
 ϕ : work function
 E : applied electric field
 q : electron charge
 ϵ_0 : permittivity of free space
 J : field-emission current density
 A : 1.54×10^{-10} (A V⁻² eV)
 B : 6.83×10^9 (V eV^{-3/2} m⁻¹)
 y : $3.7947 \times 10^{-4} E^{1/2} / \phi$
 I : field emission current
 V : applied voltage
 α : emitting area
 β : local field enhancement factor at the emitting surface

d : distance between cathode and anode
 S : slope of the F-N plot
 B_m : magnetic field
 r_c : cyclotron radius for electron orbiting in a magnetic field
 ω : microwave angular frequency
 m_e : mass of electron
 e : electron charge
 V_e : electron velocity component perpendicular to B_m
 R_g : average metal grain radius
 t : time
 Γ : a temperature-dependent parameter
 E_{to} : turn-on electric field
 E_{loc} : effective local electric field at the emitter tip
 R_t : radius of a free-standing emitter tip
 ξ : a geometric factor with a value between 1 and 5
 h : effective barrier height
 w : effective barrier width
 R_a : mean roughness
 γ : surface free energy
 f : surface stress
 G : Gibbs free energy
 ΔG^0 : change of the molar standard free energy
 $\Delta_f G^0$: standard free energy of formation
 ε : ratio of surface stress to surface free energy
 M : molecular weight
 D : average diameter of nanoparticles
 ρ : density
 T : temperature

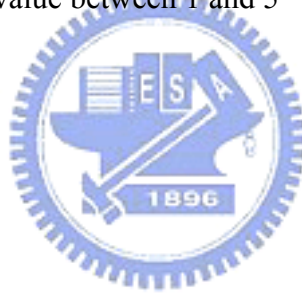


Table Caption

Table 4-1	Detailed conditions for the aluminum anodizations.....	47
Table 5-1	Experimental conditions for the CNT growth on AAO template.....	54
Table 6-1	Experimental conditions for the CNT density control on AAO template..	61
Table 7-1	Anodization conditions of the Al/TiN bilayered films for the preparation of titanium oxide nanodots.....	76



Figure Caption

Figure 1-1	Schematic drawing of the idealized structure of AAO.....	2
Figure 1-2	The allotropes of carbon: graphite, diamond, C ₆₀ , and CNTs.....	3
Figure 1-3	HRTEM image of a self-organized InAs quantum dot grown on GaAs substrate.....	4
Figure 2-1	Schematic diagram showing the electrochemical reactions and ionic paths involved during anodization of aluminum.....	7
Figure 2-2	Schematic diagram of an arc-discharge system.....	10
Figure 2-3	Schematic diagram of a laser ablation system.....	11
Figure 2-4	A photograph of a dc-PE-CVD reactor for the growth of carbon nanotubes or nanofibres.....	12
Figure 2-5	Schematic representation proposed for CNT growth from the pyrolysis of hydrocarbons on a metal particle.....	13
Figure 2-6	Image sequence of a growing carbon nanofibre.....	14
Figure 2-7	Schematic diagrams of the base-growth model.....	15
Figure 2-8	Electron micrographs of self-oriented nanotubes synthesized on n ⁺ -type porous silicon substrates.....	16
Figure 2-9	(a) An electron micrograph and (b) a schematic showing the straight/curled nanotube structure produced by an alternating plasma and thermal process. (c) is an electron micrograph showing a bundle of nanotubes with the upper portion straight and the lower portion curled.....	17
Figure 2-10	Alignment mechanism based on stress-dependent growth rate and stress distribution caused by interaction of nanotube with electric field.....	18
Figure 2-11	Electron micrographs of the cobalt-catalyzed CNTs grown out of the AAO template pores.....	19
Figure 2-12	(a) Electron micrographs of a highly order CNT array grown on AAO after ion milling, (b) top view, and (c) side view of the CNT array after the AAO template was heavily etched in HF.....	19
Figure 2-13	(A) STM topograph of strained germanium nanocrystals on silicon (001) substrate. (B) Higher magnification images of the nanocrystals.....	20
Figure 2-14	(a) Top-view SEM image of a double-well GaAs/AlGaAs quantum dot	

	array grown on GaAs (001) surface after removing the AAO template; (b) cross-sectional SEM image of a typical dot; and (c) schematic illustration of layer structure in each dot.....	21
Figure 2-15	(a) Schematic side-view of gold nanoparticles attached to a SAM by molecular wires. (b) Top-view SEM image of a self-assembled array of gold nanoparticles. Each dark dot represents a gold particle.....	22
Figure 2-16	STM image of germanium islands on the silicon (111) substrate covered with 2.9 bilayer of germanium at 450 °C. Inset shows the height profile between white arrows.....	23
Figure 2-17	Potential-energy diagram illustrating the effect of an external electric field on the energy barrier for electrons at a metal surface.....	25
Figure 2-18	Structure and SEM image of a Spindt-type field emitter.....	27
Figure 2-19	Perspective view of a Spindt-type FED in which one emitter array is shared by a red, green, and blue sub-pixel.....	29
Figure 2-20	CNT emitters formed in gated holes. Cross-section view (a), top view (b), and photograph of the anode emitting at the gate voltage of 100 V (c)....	30
Figure 2-21	Video running image of the CNT-based FED.....	31
Figure 3-1	Experimental flowchart for the fabrications and analyses of the AAO templated CNT and TiO ₂ nanodot arrays.....	32
Figure 3-2	Schematic diagram of experimental setup for the aluminum electropolishing and anodization.....	34
Figure 3-3	Schematic diagram of the microwave plasma ECR-CVD system for CNT growth.....	35
Figure 3-4	Schematic diagram of the field emission measurement setup.....	39
Figure 4-1	Contact-mode AFM images (5×5 μm ²) of the as-deposited aluminum film surface: (a) 3D diagram; (b) roughness analysis.....	41
Figure 4-2	Contact-mode AFM images (5×5 μm ²) of the aluminum film surface after the electropolishing for 7 sec: (a) 3D diagram; (b) roughness analysis....	42
Figure 4-3	Schematic diagram of the two-step anodization process.....	44
Figure 4-4	Top- or side-view FE-SEM images showing the two-step anodization process: (a) First anodization, (b) pre-textured aluminum film, and (c) second anodization and pore widening for 30 min.....	45
Figure 4-5	Cross-sectional view FE-SEM images showing (a) the aluminum oxide	

	barrier layer and (b) the vertically aligned pore channels of AAO.....	46
Figure 4-6	Anodic current density-anodizing time behaviors during the anodization of an aluminum film in a 0.3 M oxalic acid electrolyte. The insets are enlarged curve and schematic diagrams showing the anodization stages..	47
Figure 4-7	Top-view FE-SEM images of the nanoporous AAO films after the two-step anodization and pore widening. Anodization was conducted in (a) 0.3 M oxalic acid at 40 V (Sample A), (b) 0.6 M sulfuric acid at 20 V (Sample B), and 1.2 M sulfuric acid at 8 V (Sample C).....	48
Figure 4-8	Average interpore distance as a function of anodic voltage for the nanoporous AAO films.....	49
Figure 5-1	(a) Top-view FE-SEM image of the nanoporous AAO film after pore widening in a 5 vol.% phosphoric acid solution for 60 min. Cross-sectional view FE-SEM images of the AAO film (b) before and (c) after cobalt electroplating.....	53
Figure 5-2	Side-view FE-SEM images of the cobalt-catalyzed CNTs grown on the AAO template by using the ECR-CVD for (a) 7 min (sample A), (b) 15 min (sample B), and (c) 30 min (sample C). The insets show the close-up view of the CNTs grown out of the AAO template pores.....	55
Figure 5-3	(a) Cross-sectional TEM image of the very sample shown in Figure 5-2(b). The surface was covered with an amorphous silicon film to protect the exposed CNTs. (b) Electron diffraction pattern recorded from the overgrown part of the tubes shown in (a). (c) Plan-view HRTEM image of the walls of a graphitized CNT inlaid in an AAO pore.....	56
Figure 5-4	(a) Field emission current density as a function of electric field for the CNTs grown in the AAO nanopores. (b) Corresponding Fowler-Nordheim plots of the data shown in (a).....	58
Figure 6-1	Side-view FE-SEM images of the cobalt-catalyzed CNTs on AAO template grown at CH ₄ concentrations of (a) 9% (sample A), (b) 50% (sample B), and (c) 91% (sample C). The insets show the close-up view of the CNTs grown out of the AAO nanopores.....	62
Figure 6-2	(a) HRTEM image of a cobalt-catalyzed CNT shown in Figure 6-1(b). The hollow core is indicated by a dashed ellipse. (b) is the enlarged picture of the tube wall. (c) is a corresponding low magnification TEM image. The	

	square presents the magnified area of the HRTEM image.....	62
Figure 6-3	Graphitic Auger carbon (KVV) peaks of (a) an AAO assisted CNT grown at 50% CH ₄ , (b) the deposited carbonaceous film on the AAO surface grown at 91% CH ₄ , and (c) 50% CH ₄ . Reference line shapes of diamond, graphite, and amorphous carbon are provided for comparison.....	64
Figure 6-4	Raman spectra of the AAO assisted CNTs grown at (a) 9% CH ₄ , (b) 50% CH ₄ , and (c) 91% CH ₄	65
Figure 6-5	Overgrown tube length from the AAO surface as a function of CH ₄ and H ₂ concentrations.....	66
Figure 6-6	Schematic illustration of the growth model for the AAO template assisted CNTs.....	67
Figure 6-7	Tube number density of CNTs overgrown from AAO template as a function of CH ₄ and H ₂ concentrations.....	68
Figure 6-8	Field emission current density as a function of electric field for the CNTs grown on the AAO template with the three different tube densities shown in Figure 6-1.....	69
Figure 6-9	Corresponding Fowler-Nordheim plots of data shown in Figure 6-8. The slopes of the Fowler-Nordheim plot for the CNTs grown at 91% CH ₄ are also indicated in the figure.....	71
Figure 6-10	Schematic band diagram of the CNT tip with an amorphous carbon dielectric layer.....	72
Figure 7-1	Schematic diagram showing the general steps of the formation process for titanium oxide nanodots under a porous AAO film.....	75
Figure 7-2	Anodic current density-anodizing time behaviors during anodizing of the Al/TiN bilayered films in 0.3 M oxalic acid electrolyte (Sample A). The insets are schematic diagrams showing the anodization steps.....	77
Figure 7-3	(a) Cross-sectional TEM image of the bottom of AAO nanopore channels after the completion of the anodization (Sample A). (b) Diagrammatic illustration of the TEM image in (a).....	78
Figure 7-4	EELS spectra showing the titanium L _{2,3} -edge, nitrogen K-edge, and oxygen K-edge. The spectra correspond to three different positions as shown in the inset: (A) At the center, (B) at the bottom, and (C) at the underside of the titanium oxide dome (Sample A).....	79

Figure 7-5	XPS titanium 2 <i>p</i> spectra as a function of sputter time for the nanodot arrays of titanium oxides (Sample A) after the overlying AAO template was removed by wet chemical etching.....	80
Figure 7-6	Side- or top-view FE-SEM images of nanodot arrays of titanium oxides after the overlying AAO template was removed by wet chemical etching. Anodization was conducted in (a) 0.3 M oxalic acid at 40 V (Sample A), (b) 0.6 M sulfuric acid at 20 V (Sample B), and (c) 1.2 M sulfuric acid at 8 V (Sample C).....	81
Figure 7-7	Average dot diameter and interdot distance of the obtained titanium oxide nanodots as a function of anodic voltage.....	82
Figure 7-8	(a) XRD θ - 2θ scan of an epitaxial Al/TiN bilayer grown on sapphire (0001). ω -rocking curves from the (b) TiN and (c) Al layers.....	83
Figure 7-9	Cross-sectional HRTEM image of the epitaxial TiN/sapphire interface. The inset is the corresponding Fourier-filtered lattice image.....	84
Figure 7-10	Contact-mode AFM images ($1 \times 1 \mu\text{m}^2$) of the epitaxial aluminum surface: (a) 3D diagram; (b) roughness analysis.....	85
Figure 7-11	Cross-sectional TEM image of the bottom of AAO nanopore channels after the completion of the anodization of epitaxial Al/TiN bilayered films.....	86
Figure 7-12	(a) Top-view and (b) side-view FE-SEM images of the nanodot arrays of titanium oxides prepared from the epitaxial Al/TiN film stack. (c) Side-view image of the nanodots prepared from the polycrystalline film stack.....	87
Figure 7-13	The variation of the free energy difference between nanocrystalline rutile and anatase with particle diameter at 300 K.....	89
Figure 7-14	XRD θ - 2θ scan of the TiO ₂ nanodot arrays after annealing in oxygen atmosphere for 1 hour.....	90
Figure 7-15	Cross-sectional HRTEM image of the TiO ₂ nanodot/sapphire interface after annealing at 900 °C.....	91
Figure 7-16	Schematic atomic arrangements of the rutile (200) and the sapphire (0001) surfaces.....	92
Figure 8-1	Fabrication procedures of the nanodot-based field emission triodes.....	95
Figure 8-2	Top-view FE-SEM image of the titanium oxide nanodot arrays after the	

	nanoporous AAO template was removed by a mixed solution of phosphoric acid and chromic acid. The inset is the side-view image of the nanodots.....	96
Figure 8-3	Auger electron profiles of (a) an as-prepared and (b) an annealed titanium oxide nanodot presenting changes in percentage of titanium, aluminum, oxygen, and silicon atoms with the time of argon ion sputtering.....	97
Figure 8-4	Field emission current density as a function of electric field for the self-organized titanium oxide nanodot arrays after the vacuum annealing. The inset shows the corresponding Fowler-Nordheim plot.....	98
Figure 8-5	(a) Side-view FE-SEM image of the nanodot-based field emission triode array. The inset shows a higher magnification image. (b) Side-view FE-SEM image of the nanodot emitter arrays inside the gate aperture.....	100
Figure 8-6	Side-view TF-SEM image of the moveable tungsten microprobes and the field emission triode array showing the configuration for the field emission measurements. (a) Low magnification and (b) high magnification images.....	101
Figure 8-7	Gate-voltage dependence of anode and gate current. The inset shows the corresponding Fowler-Nordheim plot of the anode current.....	102

